Journal of Solid State Electrochemistry (2018) 22:3651–3661
https://doi.org/10.1007/s10008-018-4073-1

ORIGINAL PAPER

Microwave-assisted hydrothermal synthesis and electrochemical studies of α- and h-MoO_3

Galina S. Zakharova[1,2] · Christina Schmidt[1] · Alexander Ottmann[1] · Ewa Mijowska[3] · Rüdiger Klingeler[1,4]

Received: 12 March 2018 / Revised: 9 August 2018 / Accepted: 12 August 2018 / Published online: 23 August 2018

Abstract

Two modifications of molybdenum trioxide with orthorhombic (α-MoO_3) and hexagonal (h-MoO_3) crystal structure have been synthesized by a microwave-assisted hydrothermal method, facilitated by formic acid. Characterization by means of X-ray diffraction, scanning electron microscopy, specific surface analysis, and Fourier-transform infrared, Raman, and UV-Vis spectroscopy reveals phase-pure crystalline powder samples of hexagonal h-MoO_3 microrods and of α-MoO_3 nanobelt bundles, respectively. The electrochemical properties of the MoO_3 compounds, studied by cyclic voltammetry and galvanostatic cycling vs. Li/Li^+, strongly depend on the structure and the applied potential range. In the range of 1.5–3.5 V, Li^+-ions can be reversibly intercalated into the α-MoO_3 nanobelts. Utilizing the material in this way as intercalation cathode material yields an initial discharge capacity of 295 mA h g^{-1} at 100 mA g^{-1} and comparably moderate capacity fading of 25% between cycles 20 and 100. Extending the potential range to 0.01–3.0 V induces the conversion reaction to Mo, which for both modifications yields high initial capacities of around 1500 mA h g^{-1} but is associated with much stronger capacity fading.

Introduction

Molybdenum trioxide has attracted interest due to its applicability, e.g., in catalysis, gas-sensing, environmental monitoring, and lithium-ion batteries (LIBs) [1–4]. There are five known MoO_3 polymorphs: the thermodynamically stable phase of orthorhombic α-MoO_3 (space group Pbnm) and the metastable phases of monoclinic β-MoO_3 (P21/c), monoclinic β′-MoO_3 (P21/n), high-pressure monoclinic MoO_3-II or ε-MoO_3 (P21/m), and hexagonal h-MoO_3 (P63/m or P63) [5].

Among the five MoO_3 polymorphs, α-MoO_3 exhibits an orthorhombic crystal structure in which distorted MoO_6 octahedra, the universal building blocks of molybdenum trioxide, form double layers of zig-zag chains preferably along the [001] direction, sharing edges and corners, respectively (see Fig. 1). The hexagonal h-MoO_3 phase is composed of MoO_6 octahedra linked through the cis-position between adjacent chains, resulting in large one-dimensional tunnels along the [001] direction (Fig. 1). Mono- [6, 7] or bivalent cations [8] can occupy the tunnel sites, hence stabilizing the hexagonal structure of h-MoO_3. At a temperature of about 440 °C, metastable h-MoO_3 features an irreversible phase transition to the thermodynamically stable α-phase [9].

As low-dimensional structures in general facilitate Li^+ diffusion, the two-dimensionally layered α-phase has the largest potential as electrode material for LIBs among the three MoO_3 polymorphs. In α-MoO_3, lithium insertion/extraction is further supported by high chemical and mechanical stability of the host structure. Depending on the applied potential range in an electrochemical cell, there are different lithium storage mechanisms, i.e., either intercalation or conversion processes, such that α-MoO_3 can serve either as cathode or as anode material in LIBs [10–12]. At voltages above 1.5 V vs. Li/Li^+, Li^+-ion intercalation occurs without major structural changes of the layered host material,

Electronic supplementary material The online version of this article (https://doi.org/10.1007/s10008-018-4073-1) contains supplementary material, which is available to authorized users.

✉ Alexander Ottmann
alex.ottmann@kip.uni-heidelberg.de

[1] Kirchhoff Institute of Physics, Heidelberg University, INF 227, 69120 Heidelberg, Germany

[2] Institute of Solid State Chemistry, Ural Division, Russian Academy of Sciences, Yekaterinburg, Russia 620990

[3] Institute of Chemical and Environmental Engineering, West Pomeranian University of Technology, al. Piastów 45, 70-322 Szczecin, Poland

[4] Centre for Advanced Materials (CAM), Heidelberg University, INF 225, 69120 Heidelberg, Germany

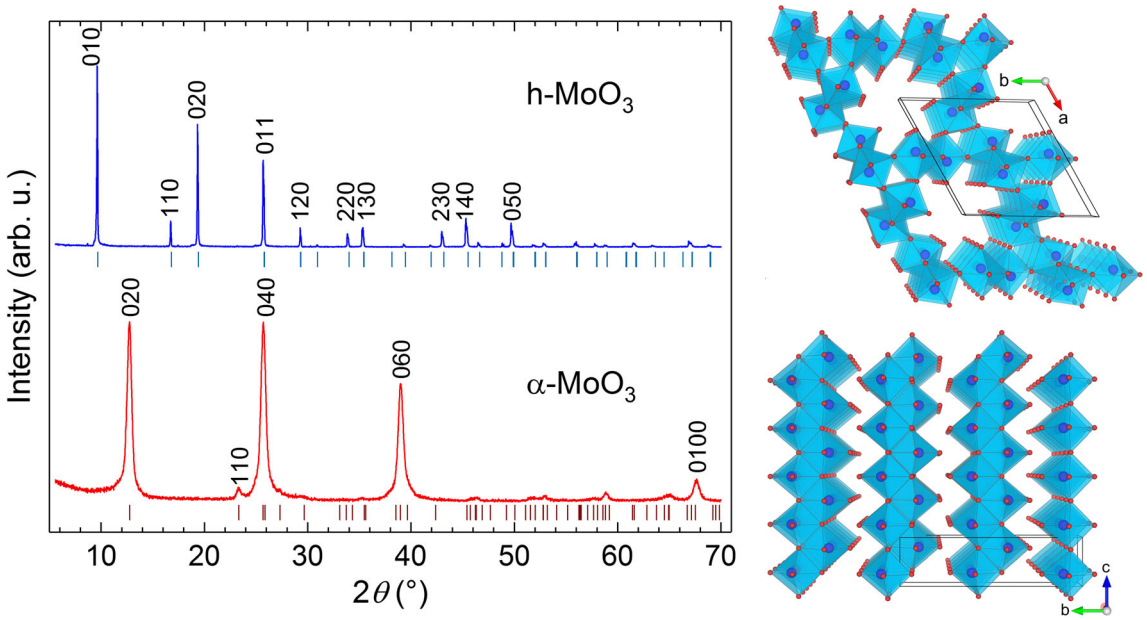

Fig. 1 XRD patterns of the h-MoO_3 and the α-MoO_3 sample (left) and schematics of the corresponding crystal structures (right)

rendering α-MoO_3 a reversible cathode material with a capacity of 186 mA h g^{-1} per intercalated Li^+-ion [13]. Changing the voltage range by cycling down to approximately 0 V vs. Li/Li^+ induces the less reversible conversion reaction to metallic Mo, which is associated with a theoretical capacity of 1117 mA h g^{-1} [14]. In contrast to α-MoO_3, electrochemical properties of h-MoO_3 have been studied in a few publications only [11, 15–17].

In general, the electrochemical performance of MoO_3 is determined by a variety of properties, such as the crystal structure, the particle size, and the morphology of the material. Several synthesis approaches have been developed, including the conventional hydrothermal [18] as well as the microwave-assisted hydrothermal method [19], ultrasonic synthesis [20], precipitation [21], solution combustion [22], and spray pyrolysis [23], what enables producing MoO_3 with, e.g., different morphologies.

Here, we develop a microwave-assisted hydrothermal route to synthesize MoO_3 of both the α- and the h-phase. One of the benefits of applying microwave radiation is fast and homogeneous heating which leads to significant shortening of the reaction time compared to the conventional approach [24]. Consequently, compounds with perceptibly different structural, morphological, and textural properties can be synthesized [25–28], even metastable phases [29]. The study at hand reports the new synthesis route and focuses on the characterization of the resultant powder materials regarding their structure, morphology, and optical and electrochemical properties.

Experimental

Synthesis

Molybdenum powder Mo (99.95% metal, Alfa Aesar), ammonium heptamolybdate tetrahydrate $(NH_4)_6Mo_7O_{24}{\cdot}4H_2O$ (81.0–83.0% MoO_3 basis, Sigma-Aldrich), hydrogen peroxide H_2O_2 (30%, Merck), and formic acid HCOOH (98–100%, Merck) were utilized for the synthesis. A typical synthetic procedure of α-MoO_3 proceeded as follows: 0.5 g of Mo powder was dissolved in 30 ml H_2O_2 at 10–15 °C to form a clear yellow solution of peroxomolybdic acid. Then, an appropriate amount (~ml) of formic acid was added dropwise under stirring to adjust the pH value to around 1.0. The obtained solution was poured into a sealed glass vial which was transferred into a microwave reactor (Monowave 300, Anton Parr). There, the reaction solution was heated to 160 °C within a ramping time of 10 min and held at this temperature for 20 min. The power of the microwave irradiation was adjusted automatically by the Monowave 300 in order to fulfill the aforementioned heating parameters, which led to an output power in the range of 0–150 W with typical values in the order of 50 W. The powdery product was separated by centrifugation and washed with deionized water several times. In order to synthesize h-MoO_3, 3.71 g of $(NH_4)_6Mo_7O_{24}{\cdot}4H_2O$ was dissolved in 100 ml of deionized water with continuous stirring at room temperature for 30 min. Subsequently, formic acid was added to the solution for adjusting the pH value to 1.5. The reactant mixture was treated similarly to the α-MoO_3 route in the microwave reactor. The obtained product was separated, washed, and dried in air under ambient conditions.

Physical characterization

X-ray diffraction (XRD) patterns were obtained on a Bruker AXS D8 Advance Eco using Cu Kα radiation with an integration step size of $\Delta 2\theta = 0.02°$. The morphology of the powder was determined by a Zeiss LEO 1530 scanning electron microscope (SEM) and a FEI Tecnai F30 transmission electron microscope (TEM). The specific surface area and pore volume of the samples were measured by a surface area and porosity analyzer (Gemine VII, Micromeritics). The chemical composition of h-MoO_3 was evaluated by means of thermogravimetric analysis (STA 449 F_3 Jupiter thermoanalyzer, Netzsch) and the Kjeldahl method. FT-IR spectra were recorded using a Bruker VERTEX 80 FT-IR spectrometer with CsI as diluting agent. Raman spectra were measured with a Renishaw U1000 spectroscope at a laser wavelength of 532 nm. UV-Vis absorption spectra were recorded on a Shimadzu UV-3600 spectrophotometer (λ = 310 nm) within the wavelength range of 190–830 nm, using barium sulfate as standard.

Electrochemistry

For the electrochemical measurements, a mixture of MoO_3 powder, carbon black (CB, Timcal), and polyvinylidenefluoride binder (PVDF, Solvay Plastics) in the weight ratio of 75:20:5 was stirred in *N*-methyl-2-pyrrolidone (NMP, Sigma-Aldrich) for 1 day. After evaporating most of the NMP at 65 °C, the resultant slurry was spread on aluminum or copper meshes, dried at 80 °C in vacuum, mechanically pressed at 10 MPa, and dried again. Two-electrode Swagelok-type cells [30] were assembled in a glove box with argon atmosphere (O_2/H_2O < 2 ppm). As counter electrode, a lithium metal foil disk (Alfa Aesar) pressed on a nickel current collector was used. The two electrodes were separated by two layers of glass microfiber (Whatman GF/D), which were soaked with 200 μl of a 1-M solution of $LiPF_6$ in ethylene carbonate and dimethyl carbonate (volume ratio 1:1) as electrolyte (Merck, LP30). Electrochemical measurements by means of cyclic voltammetry and galvanostatic cycling were performed on a VMP3 potentiostat (BioLogic) in a climate chamber at 25 °C.

Results and discussion

Structure and morphology characterization

The microwave-assisted hydrothermal synthesis approach yields crystalline powder samples of phase pure α- and h-MoO_3, respectively, as evidenced by the XRD patterns in Fig. 1. All observed Bragg peaks of both samples can be indexed in the orthorhombic Pbnm and the hexagonal $P6_3/m$ space group, respectively, according to the reference patterns of the Inorganic Crystal Structure Database #35076 [31] and #80290 [7]. Full profile analyses by means of the FullProf software, starting from the parameters of the reference patterns, yield lattice parameters of $a = 3.96(2)$ Å, $b = 13.84(2)$ Å, and $c = 3.71(2)$ Å for α-MoO_3 and $a = 10.575(3)$ Å and $c = 3.725(2)$ Å for h-MoO_3. Both crystal structures are schematically displayed in Fig. 1, highlighting their characteristic features as described in the "Introduction" section.

The morphology of the as-prepared molybdenum oxides has been examined by electron microscopy. SEM and TEM images of α-MoO_3 (Fig. 2a) reveal that the material consists of uniform nanobelts, which in large quantities are aggregated to bundles. The individual α-MoO_3 nanobelts are about 50–150 nm wide and several micrometers long. The presence of nanosized crystallites in the sample is confirmed by the XRD pattern of the α-MoO_3 material which shows significant peak broadening (Fig. 1). The analysis of the (002) peak by means of the Scherrer equation, neglecting other contributions to XRD peak broadening, yields a crystallite size of about 20 nm. The h-MoO_3 sample shows rod-like morphology with hexagonal cross section (Fig. 2b). The diameter of the rods amounts to 1–2 μm and the length is about 10–20 μm. The chemical composition of the as-prepared h-MoO_3 was

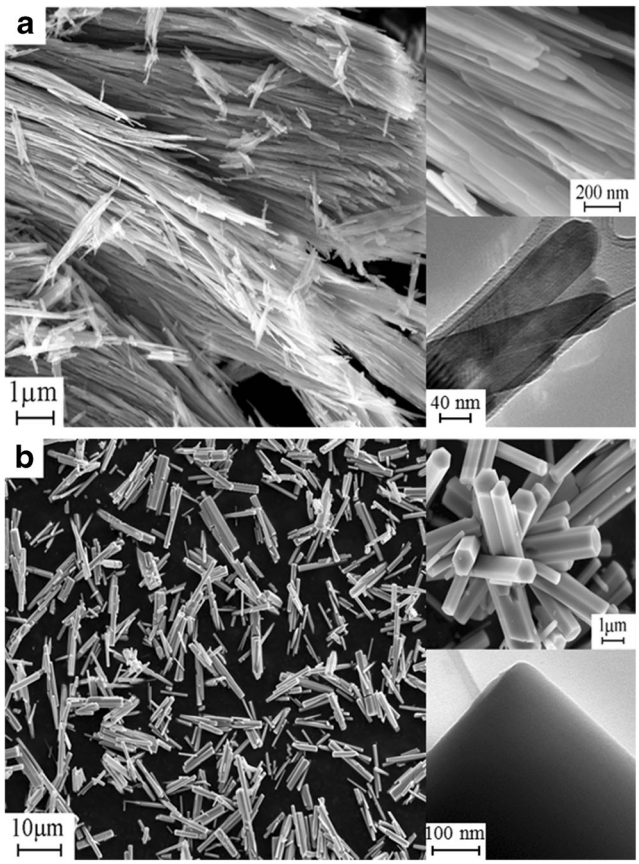

Fig. 2 SEM and TEM images of **a** α-MoO_3 nanobelts and **b** h-MoO_3 microrods

evaluated as follows: The ammonium content was determined by means of the Kjeldahl method to amount to 2.2 wt%. Furthermore, the total weight loss during thermogravimetric analysis in air up to 600 °C was 5.0 wt% (see Fig. A1). Hence, according to the molybdenum-defect model of Ref. [7], the exact composition of the presented h-MoO_3 phase can be formulated as $NH_4Mo_{5.4}O_{17.4}H_{1.4}{\cdot}0.1H_2O$. In the following, the main chemical reaction equations for the formation of both α- and h-MoO_3 are proposed. The basic reaction steps during the synthesis of α-MoO_3 nanobelts can be formulated as follows:

$$Mo + 4H_2O_2 \rightarrow MoO_2(OH)(OOH) + 3H_2O \quad (1)$$

$$MoO_2(OH)(OOH) + HCOOH \rightarrow MoO_3 + CO_2 + 2H_2O. \quad (2)$$

During the dissolution of Mo powder in H_2O_2, a peroxomolybdate solution is synthesized (Eq. (1)). The microwave-assisted hydrothermal treatment of the peroxomolybdate solution produces α-MoO_3 nanocrystals (Eq. (2)). This process is facilitated by the presence of monocarboxylic acid. Formic acid, due to its C=O bond, acts as soft reducing agent, promoting polycondensation processes and the nanoparticles' growth [32].

The key reaction for the synthesis of the h-MoO_3 microcrystals can be formally expressed as follows:

$$(NH_4)_6Mo_7O_{24}4H_2O + 6HCOOH \rightarrow 7MoO_3 + 6HCOONH_4 + 7H_2O. \quad (3)$$

A possible formation path of h-MoO_3 could be decomposed into the following reaction steps:

$$HCOOH + H_2O \rightarrow H_3O^+ + COOH^- \quad (4)$$

$$(NH_4)_6Mo_7O_{24}4H_2O \rightarrow 6NH_4^+ + Mo_7O_{24}^{6-} + 4H_2O \quad (5)$$

$$Mo_7O_{24}^{6-} + 6H^+ \rightarrow H_6Mo_7O_{24} \quad (6)$$

$$H_6Mo_7O_{24} \rightarrow 7MoO_3 + 3H_2O. \quad (7)$$

When HCOOH is added to the deionized water, an electrolytic dissociation proceeds (Eq. (4)). The $Mo_7O_{24}^{6-}$-anions are obtained by the electrolytic dissociation of isopolymolybdic acid (Eq. (5)). Arising H^+-ions support the formation of isopolymolybdic acid ($H_6Mo_7O_{24}$) according to Eq. (6). During heating under hydrothermal conditions, reaction (7) takes place and yields h-MoO_3. According to Eq. (6), a main factor for the successful synthesis of h-MoO_3 is a specific H^+-ion concentration. Usually, a mineral acid (e.g., HNO_3) is used to obtain h-MoO_3 materials [33]. In the synthesis route presented here, the required acidity is conveniently achieved by the addition of formic acid, which yields h-MoO_3 rods with smaller cross sections and larger aspect ratios of up to 20 in comparison with the samples prepared by chemical precipitation [34]. One advantage of formic acid over mineral acids could be its weak acidity.

The specific surface area and the pore size distribution of the MoO_3 materials were investigated using nitrogen adsorption–desorption isotherms (Fig. 3). According to the classification of IUPAC [35], the α-MoO_3 sample features a type-IV isotherm with a type-H1 hysteresis loop (Fig. 3a). The pore size distribution of α-MoO_3 (insert of Fig. 3a) was derived by means of the BJH method from the desorption branch of the isotherm. The obtained pore structure is complex, which can be attributed to interconnected networks of pores of different sizes. The very wide pore size distribution of the α-MoO_3 nanobelts exhibits an average pore diameter of about 33 nm. The BET specific surface area and the pore volume of the α-MoO_3 sample amount to 22.2 $m^2\ g^{-1}$ and 0.13 $cm^3\ g^{-1}$, respectively. In contrast, the h-MoO_3 sample exhibits a type-II adsorption isotherm, which is characteristic for non-porous materials (Fig. 3b). The adsorption isotherm indicates multilayer adsorption. The specific surface area and the pore volume of the h-MoO_3 microrods are very small and only amount to 1.9 $m^2\ g^{-1}$ and 0.004 $cm^3\ g^{-1}$, respectively. It is worth mentioning that the high surface area of the α-MoO_3 nanobelts and their mesoporous structure may facilitate electrolyte penetration and fast transfer of Li^+-ions upon electrochemical cycling.

Optical properties

The chemical structure of α-MoO_3 and h-MoO_3 was investigated in more detail using IR and Raman spectroscopy (Fig. 4). In the h-MoO_3 phase, NH_4^+ cations are detected, which act as a stabilizer of the hexagonal structure. Figure 4a shows the FT-IR spectra of α-MoO_3 nanobelts (red line) and h-MoO_3 microrods (blue line). In both cases, the general features are similar to what has been published for reference materials [11, 34]. The α-MoO_3 sample demonstrates three typical vibration modes. More precisely, the absorption peak at 1000 cm^{-1} indicates the symmetric stretching mode of Mo=O terminal oxygen, while the peak at 867 cm^{-1} is assigned to the asymmetric bridge stretching vibration of Mo-O-Mo bonds and the one at 533 cm^{-1} to the stretching vibration of O atoms linked to three different Mo atoms. The weak bands at 3428 and 1627 cm^{-1} are due to the stretching and bending modes of O-H, respectively, originating from trace amounts of adsorbed water in the powder. The FT-IR spectrum of h-MoO_3 shows four main peaks at 977, 919, 712, and 525 cm^{-1}. The pronounced peaks at 977 and 919 cm^{-1} are associated with stretching vibrations of Mo=O terminal oxygen. The absorption peaks at 712 and 525 cm^{-1} are assigned to the Mo-O-Mo asymmetric and symmetric stretching modes, respectively. The peaks at 3191 and 1417 cm^{-1} are due to stretching and

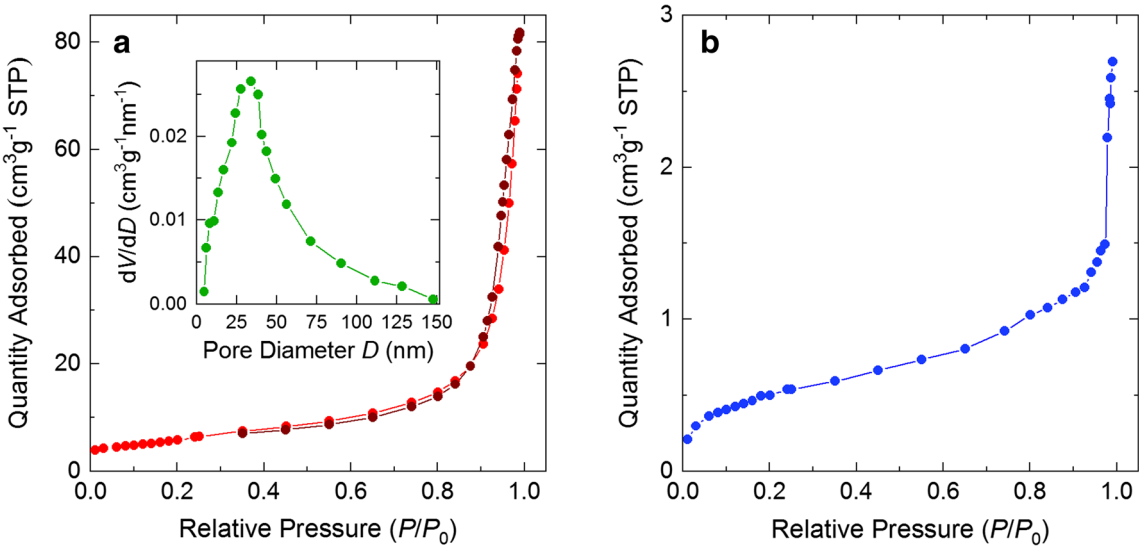

Fig. 3 Nitrogen sorption isotherms and corresponding pore size distribution curve (inset) of **a** α-MoO_3 nanobelts and **b** h-MoO_3 microrods

bending vibrations of the N-H bond of NH^{4+} ions. The broad peaks centered at 3489 and 1620 cm^{-1} correspond to stretching and bending vibrations of adsorbed water, as in the case of α-MoO_3.

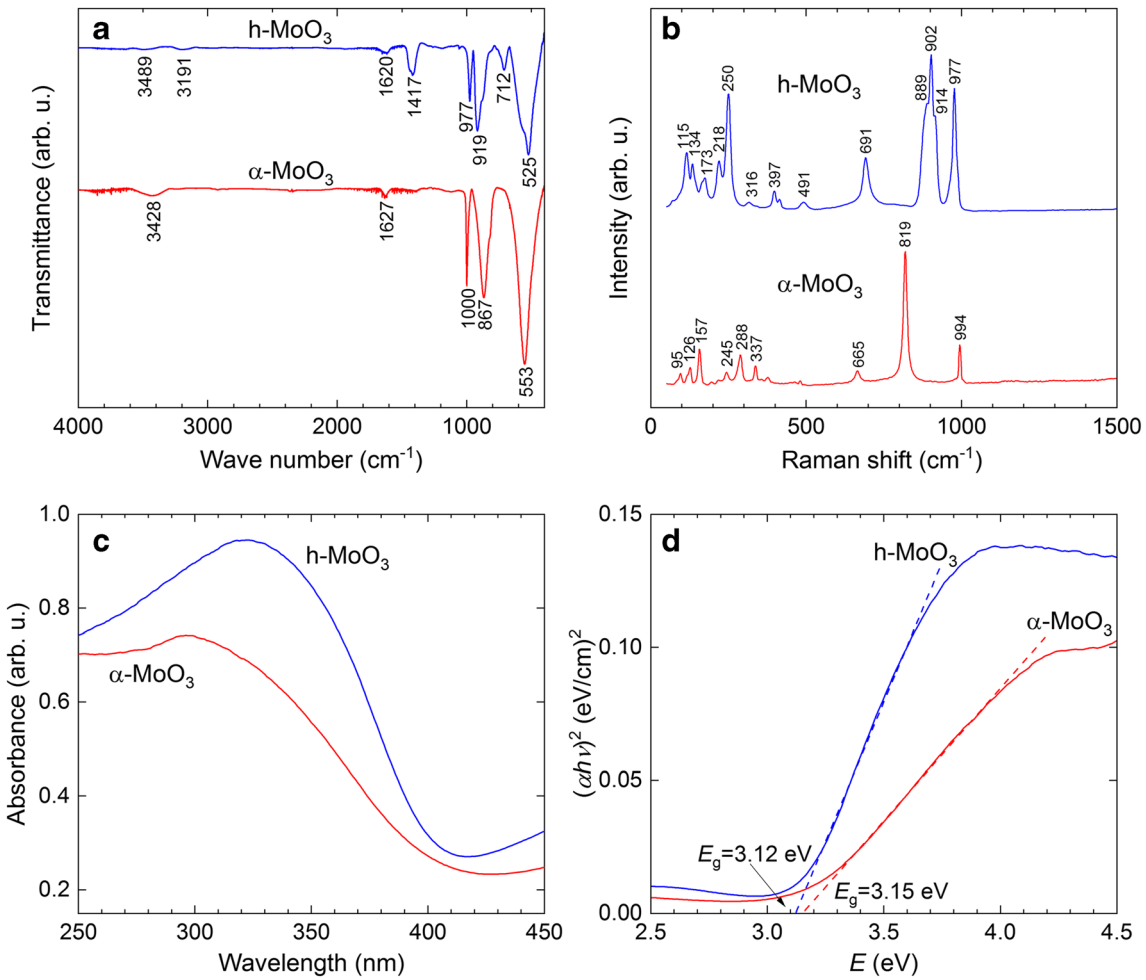

Fig. 4 **a** FT-IR, **b** Raman, and **c** UV-Vis absorption spectra with **d** plots of $(\alpha h\nu)^2$ as a function of energy E for both α-MoO_3 nanobelts and h-MoO_3 microrods

Figure 4b shows the Raman spectra of α-MoO_3 and h-MoO_3. All peaks are in good agreement with those of molybdenum oxides reported in the literature [20, 36]. In either case, the bands located below 200 cm^{-1} can be assigned to skeletal MoO_4 chain modes. The Mo-O-Mo bridge stretching vibrations are registered at 665 cm^{-1} and at 691 cm^{-1} for α-MoO_3 and h-MoO_3, respectively. Intense peaks in the range of 819–994 cm^{-1} are caused by stretching vibrations of the Mo=O bonds in the case of both phases. These vibrations are most sensitive to the presence of inserted ions in the interstitial space of the crystal structures [37, 38].

The absorption spectra and the optical band gap determination of α-MoO_3 nanobelts and h-MoO_3 microrods are shown in Fig. 4c and d, respectively. The observed optical absorption threshold around 400 nm is due to fundamental absorption and thus defined by the band gap of the materials. The optical band gap E_g, caused by charge transfer from the uppermost O2p valence band to the lowest Mo4d conduction band (O2p → Mo4d) in the $[MoO_6]^{6-}$ octahedrons, is estimated from the absorption coefficient by means of the following equation [39]:

$$(\alpha h\nu)^2 = A\left(h\nu - E_g\right) \quad (8)$$

where A is a constant, $h\nu$ is the photon energy, and E_g is the optical band gap. The linear region of the $(\alpha h\nu)^2$ vs. $E = h\nu$ graph (Fig. 4d) indicates that both MoO_3 materials under study exhibit a direct band gap. This optical band gap is determined to be 3.15(3) eV for the α-MoO_3 nanobelts, which is larger than that for the corresponding bulk material (2.9 eV) [40]. We attribute this difference to quantum size effects [41]. The estimated direct band gap E_g for the h-MoO_3 microrods amounts to 3.12(3) eV, which does not significantly differ from the α-MoO_3 nanobelts but is about 0.1 eV larger than the value reported in Ref. [37]. This slight increase in optical band gap energy for h-MoO_3 microrods is attributed to the particle size, too.

Electrochemical characterization

MoO_3 as cathode material

The electrochemical properties of the two different MoO_3 phases were examined by means of cyclic voltammetry and galvanostatic cycling as either cathode or anode material for LIBs. First, the measurements utilizing α- and h-MoO_3 as cathode materials in the potential range of 1.5–3.5 V vs. Li/Li^+ are discussed.

Figure 5 shows the cyclic voltammograms (CVs) of α-MoO_3 (a) and h-MoO_3 (b) in the 1st, 2nd, 5th, and 10th cycles. The data have been obtained at a scan rate of 0.1 mV s^{-1} after starting at open cell voltages of about 3.1 V. During the first cycle, α-MoO_3 shows two main reductive features around

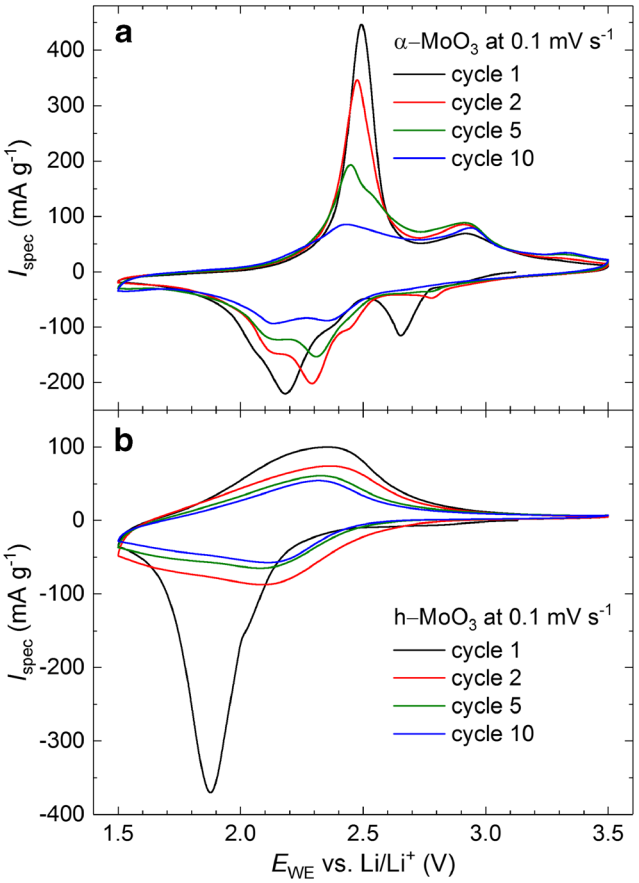

Fig. 5 Cyclic voltammograms of **a** α-MoO_3 and **b** h-MoO_3 in the 1st, 2nd, 5th, and 10th cycles, recorded in the voltage range 1.5–3.5 V at a scan rate of 0.1 mV s^{-1}

2.65 and 2.18 V as well as two oxidation peaks, i.e., a pronounced one around 2.49 V and a small one around 2.91 V (see Fig. 5a). The first, mainly irreversible reduction peak around 2.65 V indicates intercalation of Li^+-ions into the α-MoO_3 host structure up to 0.25 Li^+/f.u., leading to irreversible structural changes and the formation of a Li_xMoO_3 phase [42–46]. Upon further cycling, this peak shifts to higher potentials and completely disappears only after the eighth cycle, which implies that some of the unrecoverable lattice sites are still available for Li^+ insertion after the first cycle [47, 48]. Subsequent to the reduction process at 2.65 V, intercalation and deintercalation into/from Li_xMoO_3 up to $x \leq 1.5$ take place [43, 45, 49, 50], which is signaled by the dominant red/ox peak pair around 2.2/2.5 V in the CV (Fig. 5a). For all peaks, except the small oxidation one at 2.9 V, decreasing current intensities are found during cycling which indicates significant irreversible losses during the first 10 cycles.

The CV of h-MoO_3 (Fig. 5b) shows an irreversible reduction peak at 1.88 V in the initial cathodic scan and subsequently a partly reversible red/ox couple around 2.14/2.37 V. This reversible process can be referred to the lithiation and delithiation of MoO_3. The irreversible process might be due to irreversible changes from the hexagonally structured h-

MoO_3 to an amorphous phase caused by the insertion of Li^+-ions into the crystal lattice [15]. This is indeed supported by the comparison of the XRD patterns of a pristine and two cycled electrodes which were lithiated galvanostatically to 1.2 and 0.01 V, respectively, at a current density of 20 mA g^{-1} (Fig. A2(a) and (b)). The XRD patterns of the lithiated samples do not show any Bragg peaks related to the h-MoO_3 phase anymore, suggesting the amorphous nature of the material after just one half cycle.

The charge/discharge performances of α-MoO_3 and h-MoO_3 have been studied by galvanostatic cycling at a current density of 100 mA g^{-1}. Corresponding voltage profiles, plotted in Fig. 6a, b, respectively, exhibit plateau-like features which fully agree with the CV observations. In particular, the α-MoO_3 sample (Fig. 6a) shows two plateau regions in the first discharge (lithiation) curve, i.e., a flat one around 2.7 V followed by a slightly sloped one at 2.2–2.4 V, indicating that the first lithiation of α-MoO_3 indeed takes place in two distinguishable steps. However, in subsequent discharge curves, there is only one plateau-like feature at about 2.3 V. Upon charging, two plateaus at about 2.4 and 2.9 V are observed in all 100 cycles. For h-MoO_3, the first galvanostatic discharge curve shows one broad plateau between 2.0 and 2.2 V. In all subsequent cycles, both the discharge and charge profiles exhibit sloping regions around 2.0 and 2.3 V, respectively.

The corresponding specific capacities of α-MoO_3 and h-MoO_3 for 100 cycles at various current densities are plotted in Fig. 7. Upon employing 100 mA g^{-1}, both phases show strong capacity fading in the first cycles. Starting with an initial discharge capacity of 295 and 311 mA h g^{-1}, which corresponds to the intercalation of about 1.6 and 1.7 Li^+/f.u. for α-MoO_3 and h-MoO_3, respectively, after 20 cycles, capacities of only 147 and 78 mA h g^{-1} are found. Upon further cycling, however, the capacities show only moderate fading with capacity retentions of about 75% between cycles 20 and 100. After 100 cycles, α-MoO_3 still has a specific charge/discharge capacity of 113/108 mA h g^{-1}, whereas the one of h-MoO_3 dropped to 56/56 mA h g^{-1}. The apparently worse reversible lithium storage capability of h-MoO_3 as compared to α-MoO_3 can be ascribed to the more severe structural changes appearing upon initial lithiation. This conclusion is corroborated by much more pronounced capacity fading during the first 10 cycles.

In general, increasing the specific charge/discharge current to 300 and 1000 mA g^{-1}, respectively, leads to similar cycling stabilities with slightly lower initial discharge capacities of 256 and 222 mA h g^{-1} for α-MoO_3 as well as 293 and 251 mA h g^{-1} for h-MoO_3 (Fig. 7). Between cycles 20 and 100, α-MoO_3 shows capacity retentions of about 79 and 60%, and h-MoO_3 of 71 and 75% for 300 and 1000 mA g^{-1}, respectively.

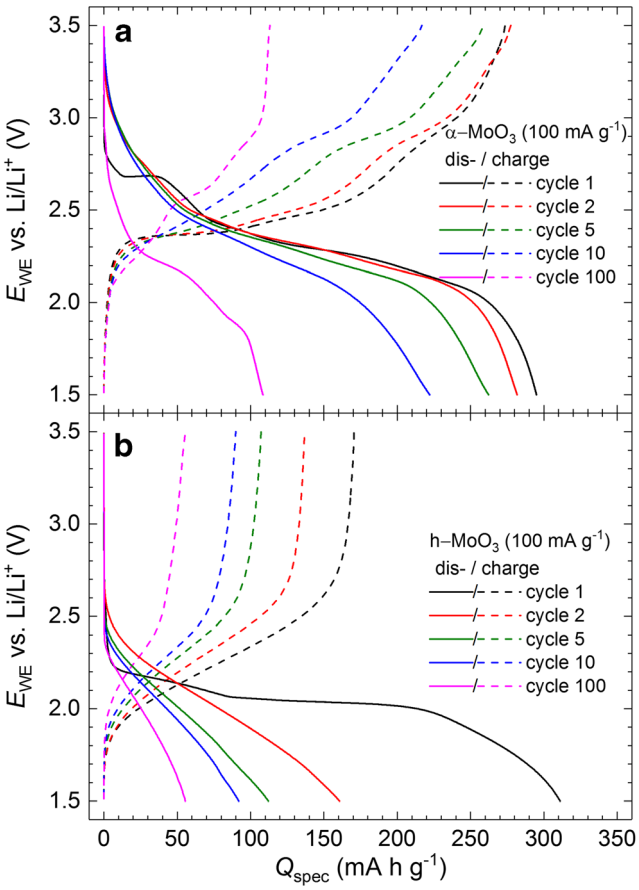

Fig. 6 Galvanostatic charge/discharge curves of **a** α-MoO_3 and **b** h-MoO_3 in the 1st, 2nd, 5th, 10th, and 100th cycles as a function of specific capacity at a current density of 100 mA g^{-1}

MoO_3 as anode material

In order to complete the electrochemical characterization of the two MoO_3 compounds, further measurements in the

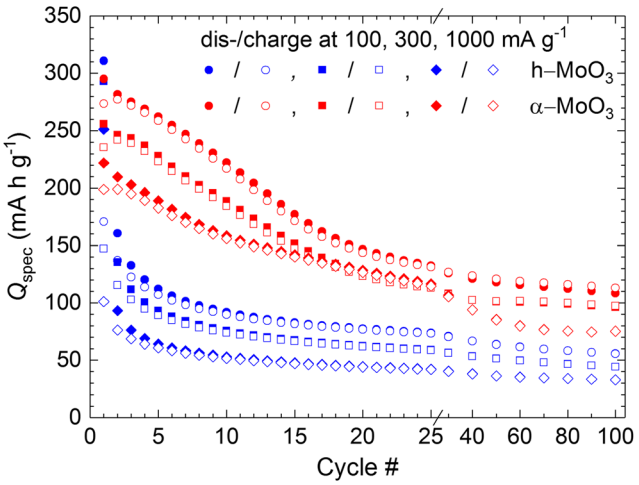

Fig. 7 Cycling stability of α-MoO_3 and h-MoO_3 within 100 cycles in the range of 1.5–3.5 V vs. Li/Li^+ at a current density of 20, 100, 300, and 1000 mA g^{-1}, respectively

potential range of 0.01–3.0 V vs. Li/Li$^+$ have been performed and refer to MoO_3 as anode material.

Figure 8 shows CVs of α-MoO_3 and h-MoO_3 in the first, second, and fifth cycles in the enlarged voltage range. In addition to the initial reduction peaks already discussed for α-MoO_3 in Fig. 5a, further redox peaks can be found in the CVs, which can be attributed to the expected conversion reaction processes. To be specific, the reduction peak at 0.18 V in the case of α-MoO_3 indicates the emergence of elemental Mo and Li_2O [11, 12, 49, 50], as well as the formation of a solid electrolyte interface (SEI) layer [14, 50, 51]. Parts of this reductive feature can also be attributed to Li$^+$ intercalation into the added carbon black with the corresponding deintercalation present at 0.4 V during the oxidative scan. Small shifts of the peaks upon cycling can be referred to lithiation-driven structural modifications [13]. The two oxidation peaks at 1.25 and 1.80 V may indicate the formation of an intermediate MoO_x phase. In the reductive scans, one additional peak at about 1.50 V appears after the first cycle, showing that different Li$^+$ sites may be available in the amorphous MoO_x phase.

For h-MoO_3 (Fig. 8b), in addition to the transformation to an amorphous phase by lithiation at 0.9 V, the data imply a conversion reaction to elemental Mo as it is indicated by the reduction peak at 0.1 V in the first cycle which shifts to 0.4 V in subsequent ones [15]. The additional reductive feature around 0.01 V originates from Li$^+$ intercalation into carbon black.

Galvanostatic cycling data shown in Fig. 9 further elucidate the differences of α-MoO_3 and h-MoO_3 as anode materials. The data agree to the CVs presented in Fig. 8. The discharge (lithiation) voltage profile of α-MoO_3 shows a distinct plateau in the first cycle at 0.4 V, which is related to the conversion process. The initial discharge capacities of α-MoO_3/h-MoO_3 of 1551/1472 mA h g^{-1} exceed the theoretical value of a complete conversion to Mo and Li_2O of 1117 mA h g^{-1}, what we attribute to the SEI formation. The following charge process is associated with capacities of 988/1011 mA h g^{-1}, thereby confirming strong irreversible contributions during the initial lithiation. After 20 cycles, the discharge capacities for α-MoO_3 and h-MoO_3 have decreased to 710 and 178 mA h g^{-1}, respectively. One of the reasons for this large decrease could be the formation of electrochemically inactive patches of material due to fractionation. After 100 cycles, α-MoO_3 still has a

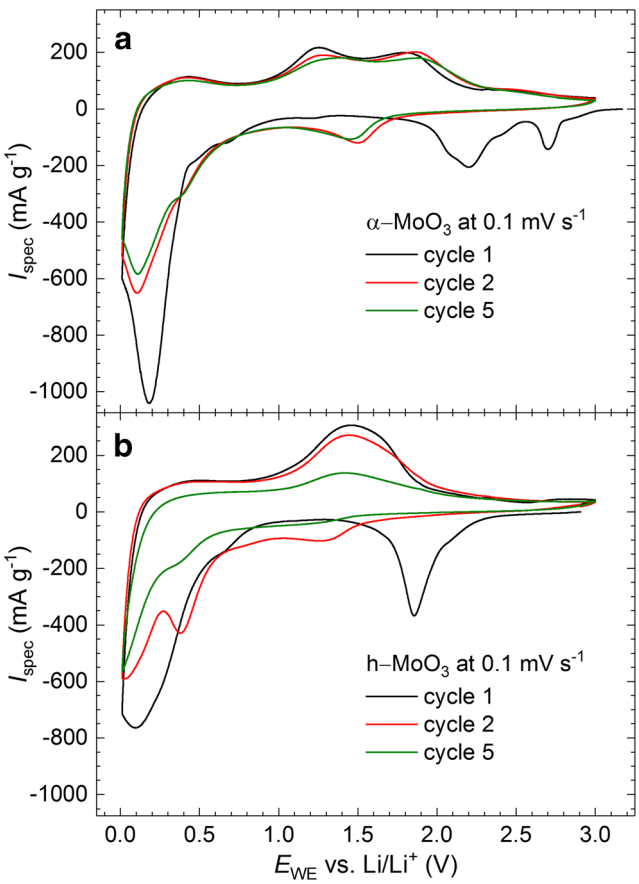

Fig. 8 Cyclic voltammograms of **a** α-MoO_3 and **b** h-MoO_3 in the 1st, 2nd, and 5th cycles, recorded in the voltage range 0.01–3.0 V at a scan rate of 0.1 mV s^{-1}

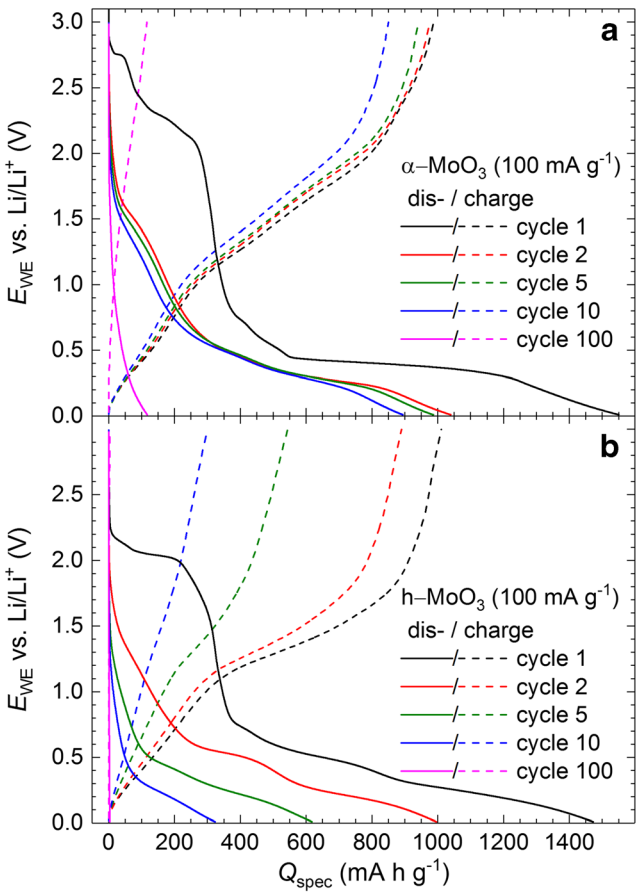

Fig. 9 Galvanostatic charge/discharge curves of α-MoO_3 **a** and h-MoO_3 **b** in the 1st, 2nd, 5th, 10th, and 100th cycles as a function of specific capacity at a current density of 100 mA g^{-1}

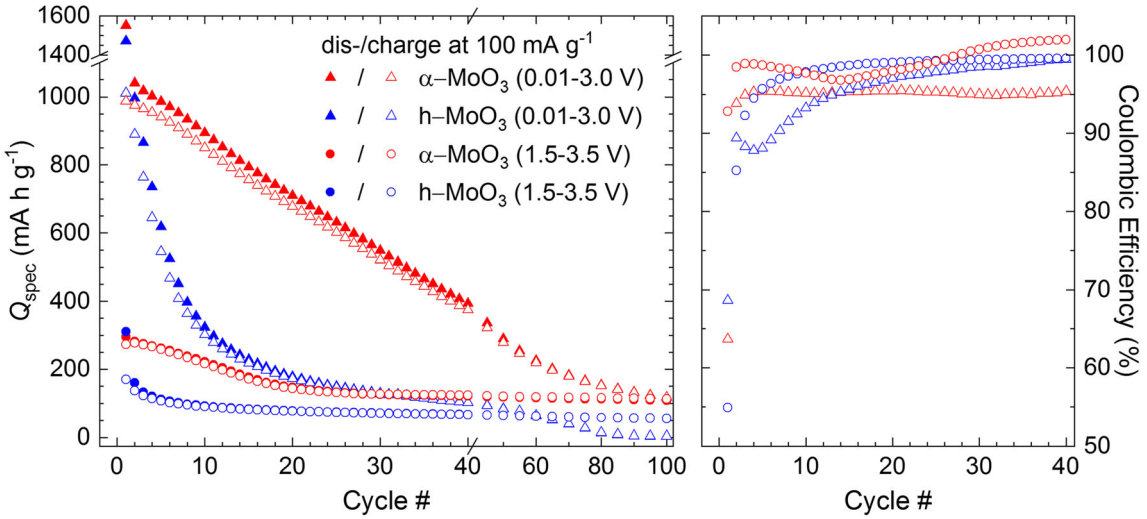

Fig. 10 Cycling stability of α-MoO_3 and h-MoO_3 in the range of 0.01–3.0 V vs. Li/Li^+ at a current density of 100 mA g^{-1} and corresponding Coulombic efficiencies

capacity of 117 mA h g^{-1}, whereas h-MoO_3 shows nearly no electrochemical activity anymore.

The cycling stability in the voltage range of 0.01–3.0 V vs. Li/Li^+ at a current density of 100 mA g^{-1} is compared with the data at 1.5–3.5 V in Fig. 10, also showing the corresponding Coulombic efficiencies. In both voltage ranges, during the first 10 cycles, the specific capacities of h-MoO_3 decrease much more than those of α-MoO_3, which is associated with considerably worse Coulombic efficiencies. For instance, between cycles 1 and 10, α-MoO_3 exhibits average efficiencies of 98% and 92% for the voltage ranges 1.5–3.5 and 0.01–3.0 V, respectively, compared to 91% and 88% in case of h-MoO_3. These values also demonstrate that there are less irreversible losses when both MoO_3 compounds are cycled as cathode materials between 1.5 and 3.5 V. While the discharge capacity of α-MoO_3 converges to a value of about 115 mA g^{-1} with a capacity retention of 92% as cathode material between cycles 30 and 100, h-MoO_3 shows a capacity of only 58 mA g^{-1} after cycle 80.

The presented electrochemical studies on pristine α-MoO_3 and h-MoO_3, both being synthesized under similar conditions, yield two main conclusions: (1) α-MoO_3 is better suited for reversible electrochemical Li^+ storage than h-MoO_3, which can be linked to the inferior structural stability of h-MoO_3, in particular during electrochemical cycling [11]; (2) utilizing MoO_3 as cathode (1.5–3.5 V) rather than as anode material (0.01–3.0 V) for LIBs results in better cycling stabilities, which confirms larger irreversibility during conversion to elemental Mo as compared to the intercalation process into MoO_3. In fact, α-MoO_3 can be modified, e.g., by Na^+ pre-intercalation [52] or by oxygen vacancies in the MoO_3 structure [53], to exhibit very promising Li^+ storage properties at voltages above 1.5 V vs. Li/Li^+.

Conclusions

In summary, we report the microwave-assisted hydrothermal synthesis of orthorhombic (α-MoO_3) and hexagonal (h-MoO_3) molybdenum trioxide and discuss possible reaction pathways. The physical characterization reveals phase-pure crystalline powder samples of hexagonal h-MoO_3 microrods and of α-MoO_3 nanobelt bundles. Electrochemical studies in different voltage ranges enable investigating the reversible intercalation process at 1.5–3.5 V. We find an initial discharge capacity of 295 mA h g^{-1} at 100 mA g^{-1} and comparably moderate capacity fading of 25% between cycles 20 and 100 for α-MoO_3. In the extended potential range down to 0.01 V, the conversion reaction to Mo is studied for both modifications. It exhibits high initial capacities of around 1500 mA h g^{-1} but is associated with much stronger capacity fading as found in the cathodic regime. Our results show that the layered structure of α-MoO_3 promotes better Li^+ transfer kinetics while the hexagonal structure of h-MoO_3 rapidly converts into an amorphous one upon electrochemical cycling. Accordingly, while h-MoO_3 does not qualify for electrochemical energy storage, α-MoO_3 is a promising intercalation material for LIBs.

Data availability The datasets generated during and/or analyzed during the current study are available from the corresponding author on reasonable request.

Acknowledgements GZ acknowledges support by the UD RAS project No. 18-10-3-32. GZ acknowledges financial support by the Excellence Initiative of the German Federal Government and States. AO and RK are grateful to the CleanTech-Initiative of the Baden-Württemberg-Stiftung (Project CT-3 Nanostorage). Support by the Deutsche Forschungsgemeinschaft via project KL1824/12-1 is acknowledged.

Compliance with ethical standards

Conflict of interest The authors declare that they have no conflict of interest.

References

1. Bai H, Yi W, Li J, Xi G, Li Y, Yang H, Liu J (2016) Direct growth of defect-rich $MoO_{(3-x)}$ ultrathin nanobelts for efficiently catalyzed conversion of isopropyl alcohol to propylene under visible light. J Mater Chem A 4(5):1566–1571
2. Zheng Q, Huang J, Cao S, Gao H (2015) A flexible ultraviolet photodetector based on single crystalline MoO_3 nanosheets. J Mater Chem C 3(28):7469–7475
3. Yang S, Liu Y, Chen W, Jin W, Zhou J, Zhang H, Zakharova GS (2016) High sensitivity and good selectivity of ultralong MoO_3 nanobelts for trimethylamine gas. Sens Actuators B: Chem 226: 478–485
4. Wang F, Xiao S, Hou Y, Hu C, Liu L, Wu Y (2013) Electrode materials for aqueous asymmetric supercapacitors. RSC Adv 3(32):13059–13084
5. Lunk H-J, Hartl H (2017) Discovery, properties and applications of molybdenum and its compounds. ChemTexts 3(3):13
6. Olenkova IP, Plyasova LM, Kirik SD (1981) Crystal structure of "hexagonal" MoO_3. React Kinet Catal Lett 16(1):81–85
7. Guo J, Zavalij P, Whittingham MS (1995) Metastable hexagonal molybdates: hydrothermal preparation, structure, and reactivity. J Solid State Chem 117(2):323–332
8. Zakharova GS, Volkov VL, Täschner C, Hellmann I, Klingeler R, Leonhardt A, Büchner B (2011) Synthesis, characterization and magnetic properties of hexagonal $(VO)_{0.09}V_{0.18}Mo_{0.82}O_3{\cdot}0.54H_2O$ microrods. Mater Lett 65(3): 579–582
9. Liu Y, Yang S, Lu Y, Podval'naya NV, Chen W, Zakharova GS (2015) Hydrothermal synthesis of h-MoO_3 microrods and their gas sensing properties to ethanol. Appl Surf Sci 359:114–119
10. Hu X, Zhang W, Liu X, Mei Y, Huang Y (2015) Nanostructured Mo-based electrode materials for electrochemical energy storage. Chem Soc Rev 44(8):2376–2404
11. Huang J, Yan J, Li J, Cao L, Xu Z, Wu J, Zhou L, Luo Y (2016) Assembled-sheets-like MoO_3 anodes with excellent electrochemical performance in Li-ion battery. J Alloys Compd 688:588–595
12. Nadimicherla R, Zha R, Wei L, Guo X (2016) Single crystalline flowerlike α-MoO_3 nanorods and their application as anode material for lithium-ion batteries. J Alloys Compd 687:79–86
13. Gao B, Fan H, Zhang X (2012) Hydrothermal synthesis of single crystal MoO_3 nanobelts and their electrochemical properties as cathode electrode materials for rechargeable lithium batteries. J Phys Chem Solids 73(3):423–429
14. Yang Q-D, Xue H-T, Xia-Yang GZ, Cheng Y, Tsang S-W, Lee C-S (2015) Low temperature sonochemical synthesis of morphology variable MoO_3 nanostructures for performance enhanced lithium ion battery applications. Electrochim Acta 185:83–89
15. Zhou J, Lin N, Wang L, Zhang K, Zhu Y, Qian Y (2015) Synthesis of hexagonal MoO_3 nanorods and a study of their electrochemical performance as anode materials for lithium-ion batteries. J Mater Chem A 3(14):7463–7468
16. Song J, Wang X, Ni X, Zheng H, Zhang Z, Ji M, Shen T, Wang X (2005) Preparation of hexagonal-MoO_3 and electrochemical properties of lithium intercalation into the oxide. Mater Res Bull 40(10): 1751–1756
17. Tang Q, Wang L, Zhu K, Shan Z, Qin X (2013) Synthesis and electrochemical properties of H-MoO_3/graphene composite. Mater Lett 100:127–129
18. Chithambararaj A, Bose AC (2011) Hydrothermal synthesis of hexagonal and orthorhombic MoO_3 nanoparticles. J Alloys Compd 509(31):8105–8110
19. Phuruangrat A, Ham DJ, Thongtem S, Lee JS (2009) Electrochemical hydrogen evolution over MoO_3 nanowires produced by microwave-assisted hydrothermal reaction. Electrochem Commun 11(9):1740–1743
20. Bai S, Chen S, Chen L, Zhang K, Luo R, Li D, Liu CC (2012) Ultrasonic synthesis of MoO_3 nanorods and their gas sensing properties. Sens Actuators B: Chem 174:51–58
21. Jittiarporn P, Sikong L, Kooptarnond K, Taweepreda W (2014) Effects of precipitation temperature on the photochromic properties of h-MoO_3. Ceram Int 40(8):13487–13495
22. Parviz D, Kazemeini M, Rashidi AM, Jafari Jozani K (2010) Synthesis and characterization of MoO_3 nanostructures by solution combustion method employing morphology and size control. J Nanopart Res 12(4):1509–1521
23. Boudaoud L, Benramdane N, Desfeux R, Khelifa B, Mathieu C (2006) Structural and optical properties of MoO_3 and V_2O_5 thin films prepared by spray pyrolysis. Catal Today 113(3-4):230–234
24. Bilecka I, Niederberger M (2010) Microwave chemistry for inorganic nanomaterials synthesis. Nanoscale 2(8):1358–1374
25. Neef C, Jähne C, Meyer H-P, Klingeler R (2013) Morphology and agglomeration control of $LiMnPO_4$ micro- and nanocrystals. Langmuir 29(25):8054–8060
26. Cho S, Jung S-H, Lee K-H (2008) Morphology-controlled growth of ZnO nanostructures using microwave irradiation: from basic to complex structures. J Phys Chem C 112(33):12769–12776
27. Hu X, Yu JC (2008) Continuous aspect-ratio tuning and fine shape control of monodisperse α-Fe_2O_3 nanocrystals by a programmed microwave–hydrothermal method. Adv Funct Mater 18(6):880–887
28. Park S-E, Chang J-S, Hwang YK, Kim DS, Jhung SH, Hwang JS (2004) Supramolecular interactions and morphology control in microwave synthesis of nanoporous materials. Catal Surv Jpn 8(2): 91–110
29. Jähne C, Neef C, Koo C, Meyer H-P, Klingeler R (2013) A new $LiCoPO_4$ polymorph via low temperature synthesis. J Mater Chem A 1(8):2856
30. Popa AI, Vavilova E, Täschner C, Kataev V, Büchner B, Klingeler R (2011) Electrochemical behavior and magnetic properties of vanadium oxide nanotubes. J Phys Chem C 115(13):5265–5270
31. Kihlborg L (1963) Least squares refinement of crystal structure of molybdenum trioxide. Arkiv Kemi 21:357
32. Zakharova GS, Täschner C, Volkov VL, Hellmann I, Klingeler R, Leonhardt A, Büchner B (2007) $MoO_{3-\delta}$ nanorods: synthesis, characterization and magnetic properties. Solid State Sci 9(11): 1028–1032
33. Chithambararaj A, Chandra Bose A (2014) Role of synthesis variables on controlled nucleation and growth of hexagonal molybdenum oxide nanocrystals: investigation on thermal and optical properties. CrystEngComm 16(27):6175–6186
34. Song J, Ni X, Gao L, Zheng H (2007) Synthesis of metastable h-MoO_3 by simple chemical precipitation. Mater Chem Phys 102(2-3):245–248
35. Sing KSW, Everett DH, Haul RAW, Moscou L, Pierotti RA, Rouquerol J, Siemieniewska T (1985) Reporting physisorption data for gas/solid systems with special reference to the determination of surface area and porosity. Pure Appl Chem 57(4):603–619
36. Phuruangrat A, Chen JS, Lou XW, Yayapao O, Thongtem S, Thongtem T (2012) Hydrothermal synthesis and electrochemical properties of α-MoO_3 nanobelts used as cathode materials for Li-ion batteries. Appl Phys A Mater Sci Process 107(1):249–254

37. Pan W, Tian R, Jin H, Guo Y, Zhang L, Wu X, Zhang L, Han Z, Liu G, Li J, Rao G, Wang H, Chu W (2010) Structure, optical, and catalytic properties of novel hexagonal metastable h-MoO_3 nano- and microrods synthesized with modified liquid-phase processes. Chem Mater 22(22):6202–6208
38. Zhang CC, Zheng L, Zhang ZM, Dai RC, Wang ZP, Zhang JW, Ding ZJ (2011) Raman studies of hexagonal MoO_3 at high pressure. Phys Status Solidi B 248(5):1119–1122
39. Tauc J (1966) The optical properties of solids. Academic, Waltham
40. Hu H, Deng C, Xu J, Zhang K, Sun M (2015) Metastable h-MoO_3 and stable α-MoO_3 microstructures: controllable synthesis, growth mechanism and their enhanced photocatalytic activity. J Exp Nanosci 10(17):1336–1346
41. Alivisatos AP (1996) Perspectives on the physical chemistry of semiconductor nanocrystals. J Phys Chem 100(31):13226–13239
42. Dickens PG, Reynolds GJ (1981) Transport and equilibrium properties of some oxide insertion compounds. Solid State Ionics 5:331–334
43. Besenhard J, Heydecke J, Fritz H (1982) Characteristics of molybdenum oxide and chromium oxide cathodes in primary and secondary organic electrolyte lithium batteries I: morphology, structure and their changes during discharge and cycling. Solid State Ionics 6(3):215–224
44. Besenhard JO, Heydecke J, Wudy E, Fritz HP, Foag W (1983) Characteristics of molybdenum oxide and chromium oxide cathodes in primary and secondary organic electrolyte lithium batteries II: transport properties. Solid State Ionics 8(1):61–71
45. Spahr ME, Novák P, Haas O, Nesper R (1995) Electrochemical insertion of lithium, sodium, and magnesium in molybdenum (VI) oxide. J Power Sources 54(2):346–351
46. Tsumura T, Inagaki M (1997) Lithium insertion/extraction reaction on crystalline MoO_3. Solid State Ionics 104(3-4):183–189
47. Sen UK, Mitra S (2012) Electrochemical activity of α-MoO_3 nanobelts as lithium-ion battery cathode. RSC Adv 2(29):11123
48. Li W, Cheng F, Tao Z, Chen J (2006) Vapor-transportation preparation and reversible lithium intercalation/deintercalation of alpha-MoO_3 microrods. J Phys Chem B 110(1):119–124
49. Wang Z, Madhavi S, Lou XW (2012) Ultralong α-MoO_3 nanobelts: synthesis and effect of binder choice on their lithium storage properties. J Phys Chem C 116(23):12508–12513
50. Yuan Z, Si L, Wei D, Hu L, Zhu Y, Li X, Qian Y (2014) Vacuum topotactic conversion route to mesoporous orthorhombic MoO_3 nanowire bundles with enhanced electrochemical performance. J Phys Chem C 118(10):5091–5101
51. Xue X-Y, Chen Z-H, Xing L-L, Yuan S, Chen Y-J (2011) SnO_2/alpha-MoO_3 core-shell nanobelts and their extraordinarily high reversible capacity as lithium-ion battery anodes. Chem Commun 47(18):5205–5207
52. Dong Y, Xu X, Li S, Han C, Zhao K, Zhang L, Niu C, Huang Z, Mai L (2015) Inhibiting effect of Na^+ pre-intercalation in MoO_3 nanobelts with enhanced electrochemical performance. Nano Energy 15:145–152
53. Kim H-S, Cook JB, Lin H, Ko JS, Tolbert SH, Ozolins V, Dunn B (2017) Oxygen vacancies enhance pseudocapacitive charge storage properties of MoO_{3-x}. Nat Mater 16(4):454–460